A single-input state-switching building block harnessing internal instabilities

ten Wolde, Malte A.; Farhadi, Davood

DOI
10.1016/j.mechmachtheory.2024.105626

Publication date
2024

Document Version
Final published version

Published in
Mechanism and Machine Theory

Mechanism and Machine Theory 196 (2024) 105626

Contents lists available at ScienceDirect

Mechanism and Machine Theory

journal homepage: www.elsevier.com/locate/mechmt

Research paper

A single-input state-switching building block harnessing internal instabilities

Malte A. ten Wolde, Davood Farhadi *

Delft University of Technology, Department of Precision and Microsystem Engineering, Mekelweg 2, Delft, 2628 CD, The Netherlands

ARTICLE INFO

Keywords:
Bistable mechanism
Compliant mechanism
State switching
Mechanical computing
Elastic instability

ABSTRACT

Bistable mechanisms are prevalent across a broad spectrum of applications due to their ability to maintain two distinct stable states. Their energy consumption is predominantly confined to the process of state transitions, thereby enhancing their efficiency. However, the transition often requires two distinct digital inputs, implicating the requirement of multiple actuators. Here, we propose an elastic and contactless design strategy for inducing state transitions in bistable mechanisms, requiring only a single digital input. The strategy leverages internal information, interpreted as system state, as an extra input to make a weighted decision for transitioning to the subsequent state. We characterize the behavior using a spring-based rigid-body model, consisting of a column near bifurcation, combined with a non-linear spring connected to a bistable element that represents the information state. The results show that a nonlinear spring with a quadratic stiffness function, i.e., representing internal instability, is crucial for regulating state-switching behavior. We then demonstrate this design strategy by developing a monolithic and compliant design embodiment and experimentally evaluate its behavior.

1. Introduction

Bistable mechanisms have two stable equilibrium states, separated by an energy barrier. The transition from one stable state to the other is often a snap-through action, resulting in a large elastic deformation of the mechanism. These deformations consume power only when switching between the two states. These properties make bistable mechanisms suitable for various applications across numerous fields [1,2], including, but not limited to, robotics [3,4], reprogrammable mechanical metamaterials [5,6], multistable auxetic structures [7–9], mechanical waveguides [10], mechanical logic elements [11–14], energy absorbers [15], and microscale electromechanical systems (MEMS) like micro-positioners [16], actuators [17], grippers [18], optical switches [19], mechanical relays [20], micro-fluidic valves [21], as well as nanoscale applications such as DNA-based structures [22–24].

The transition between the states of a bistable element, namely state-0, and state-1, can be initiated by an external input caused by sources such as a change in temperature, pressure, voltage, or mechanical forces. Conventionally this transition requires two input displacements with opposite directions, e.g. a positive pressure for transition to state-1, and a negative pressure for transition to state-0. In other words, the sign of the input displacement must change to transition between the two states, necessitating two distinct digital inputs for state transition [25].

For example, bistable Kresling origami modules can use positive and negative pressure to demonstrate multimodal deformation [26] or use compression and tension to access the two states and thereby achieve peristaltic locomotion [27]. Another example can be found in Ionic polymer–metal composite (IMPC) actuators that use positive and negative voltages to switch between two

* Corresponding author.
E-mail address: d.farhadimachekposhti@tudelft.nl (D. Farhadi).

https://doi.org/10.1016/j.mechmachtheory.2024.105626
Received 19 September 2023; Received in revised form 15 February 2024; Accepted 8 March 2024
Available online 16 March 2024

states and enable motion for untethered miniature robots [28]. Additionally, manual resets are commonly used in various contexts, such as in mechanical signal propagation within soft media [29] and multistable surfaces [6,30].

For a system with a single bistable unit, the requirement for two distinct digital inputs can be manageable. However, the implementation becomes more challenging in complex structures that utilize multistability to achieve multiple functionalities or properties [5,30,31]. These systems, leveraging numerous stable states, require sophisticated actuation [32] or control schemes [26] for state transitions. To reduce the complexity, an alternative approach involves the implementation of adaptive structures [33,34], where internal information serves as an additional input for state transition. For example, recently a pneumatically actuated soft robot demonstrated the ability to walk and switch gaits to control the direction of locomotion using only a single constant source of pressurized air [35]. This efficiency is achieved by delegating some of the decision-making capabilities in state transition to the mechanism itself [36–38]. Unlike conventional systems, adaptive systems do not solely rely on external inputs but integrate internal information – such as mechanical memory or state information – into the state transition process. Here, the input signal can remain identical, i.e., amplitude and direction, while the current state of the system becomes the criterion for effecting transitions between states. This shift towards state-dependent transitions offers a promising direction for simplifying the input in highly multistable systems. This implies that adaptive bistable mechanisms could function with only a single digital input, i.e., a positive displacement push-on push-off mechanism, without the need for a negative displacement as a counter input.

Developing adaptive systems requires a building block that combines an external input with internal information when making a decision. Some research has been conducted to achieve this functionality. A well-known example is the mechanism in retractable ballpoint pens [39], which is an angled tooth cam following mechanism consisting of discrete parts. When the input is pressed repeatedly, the current state of the system (ballpoint in or out) determines the next state. Generally, this functionality can be found in single-input switches, for example in MEMS devices [25,40–43]. Furthermore, this functionality has been realized through different methodologies within the field of mechanical metamaterials [44,45]; one such approach involves a unit cell consisting of two inward buckling beams with a carefully designed cutout, and a central ‘state’ beam in which its buckling direction changes when interacting with the inward buckling beams upon a cyclic input displacement [46]. Separate studies have demonstrated how coupled interaction between unit cells, i.e., repeated building blocks in a structure like waves in corrugated sheets [47] or domes in a dome-patterned sheet [48], can change the response depending on their current global state. In yet another example, researchers leverage geometric frustration [49] to exhibit a history-dependent response, i.e., indicating that a system’s past states influence its present and future behavior [50].

Although there have been significant advancements in the design of these types of systems, current solutions have several limitations that hinder their performance and usability. For instance, many existing designs rely on contact-based switching that have hysteresis, displacement errors due to manufacturing tolerances, and are prone to wear due to friction, which results in a loss of information from the input. Furthermore, since most the state of the art solutions are contact-based, they all face problems when scaling down due to micro-stiction [51]. Additionally, unit cells with coupled interactions are often not rationally designed, making it difficult to predict how these coupled interactions work when increasing the number of state unit cells for more complex computations. Furthermore, some designs, such as those that utilize mechanically frustrated unit cells, can only compute once before having to reset manually, reducing their flexibility and versatility in real applications.

To achieve a fully elastic, i.e., compliant, and contact-less device for converting a cyclic digital input into two distinct output motions, kinematics with a limited range of motion are required. This would allow classical hinges to be later translated into compliant ones [52]. However, such a function encounters a force transmission issue and changes in degrees of freedom due to kinematic singularity [53,54]. In other words, upon a given input displacement, two different motion paths, i.e., bifurcation path, must be possible. This results in situations where the input experiences zero velocity in any given kinematic chain. In particular, this relates to scenarios where two overlapping serial kinematic singularity configurations are evident [55].

In this paper, we propose a fully elastic and contactless state-switching building block, that harnesses internal instabilities to switch between two distinct states in response to a single digital input. In the following sections, we will discuss the details of our proposed building block. In Section 2, we will describe the design principle behind the mechanism, including an analytical spring-based rigid-body model. Section 3 covers an analytical case study used to evaluate its performance, where the two design parameters of the nonlinear spring are studied. In Section 4, we propose a planar design embodiment and cover the numerical simulations, fabrication, and experimental validation of our prototype. Then, in Section 5, the results of the simulations and measurements are presented. Furthermore, we provide a discussion and interpretation of our findings. Section 6 will provide a discussion on opportunities and potential future research directions. Finally, in Section 7, we present our conclusion.

2. Design principle

To regulate state switching in bistable mechanisms, we propose a building block consisting of three elements. This includes a state element, a buckling column initially configured around bifurcation, and a connecting spring that connects the two, see Fig. 1A. The building block represents two distinct states, e.g. ‘state-0’ and ‘state-1’, that alternate with a single digital input displacement. A bistable mechanism, with two stable equilibrium positions, is used to represent the two states. The force–displacement characteristic of such an element is shown in Fig. 1B; with state displacement d_s between the two different stable states, and critical loads $F_{cr,1}$ and $F_{cr,2}$. The bistable element requires pull and push input to switch between the two states. The buckling column is configured such that it can buckle in two directions, and can convert a compression input, u_{in}, into a pull and push motion along the x-axis, see Fig. 1A (2) and (4) respectively. Lastly, the connecting spring, shown with k_n, has two functions to achieve the alternating behavior. Firstly, controlling the response by reading the current state of the state element, see Fig. 1A (1) and (3), and secondly, switching the state

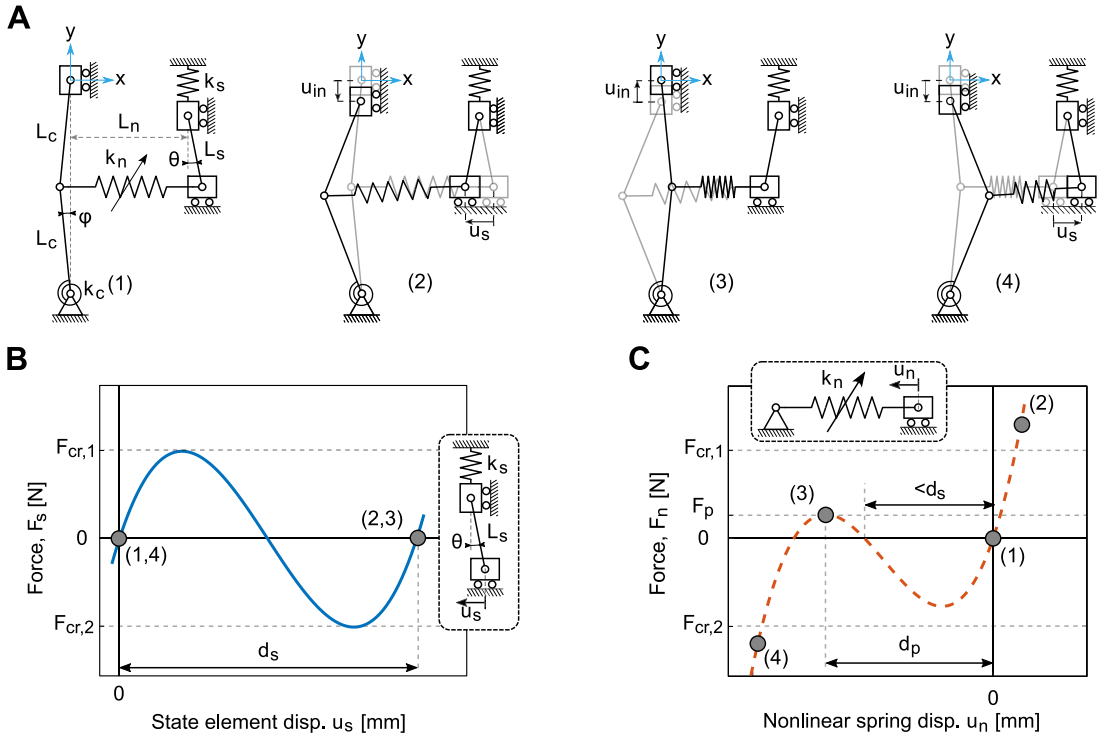

Fig. 1. Design methodology for single digital input state-switching building block. The building block consists of a state element, a buckling column near bifurcation, and a nonlinear spring connecting the two. (A) Four configurations of the mechanism representing the states and state-transitions: initial stable state-0 (1), state-transition from 0 to state-1 (2), stable state-1 (3), resetting state-transition (4). (B) The force–displacement characteristics of a state element. (C) One possible solution for the force–displacement characteristics of the nonlinear spring (dashed line), crossing the four key points related to the four configurations: initial conditions as fabrication (1), required tensile forces in configurations (2) and (3) to pull the buckling column to the other bifurcation path, and a compressive force in configuration (4).

(writing) by transmitting the input force towards the state element, see Fig. 1A (2) and (4). To achieve this, the spring characteristics should be highly nonlinear and meet specific design requirements. First, we address the force–displacement requirements related to the four configurations displayed in Fig. 1A, and then we discuss the continuous force–displacement characteristics and stiffness of the nonlinear spring.

The connecting spring has force–displacement criteria related to each of the configurations (1) to (4), see circles labeled (1) to (4) in Fig. 1C, that depends on the state element and the buckling column. In the initial configuration, the system is stable, thus the displacement $u_n = 0$ and force $F_n = 0$; this is represented as configuration (1). In addition, the buckling column is designed with an imperfection, i.e., a small initial angle ϕ_0, such that the left buckling bifurcation path is preferred when an input u_{in} is given. In configuration (2), when the input displacement is maximal, $u_{in} = U_{max}$, the tension in the connecting spring should exceed the critical load of $F_{cr,1}$, so that the state element snaps-through to state-1. In configuration (3), the connecting spring should deliver a tensile force denoted as F_p. This force should be equal to or greater than the force generated by the hinges of the buckling column, with stiffness k_c, when rotating the buckling column to $\phi = -\phi_0$. This ensures that the buckling direction of the column is in the positive x-direction. By designing the connecting spring such that the spring is still in tension when it is shortened due to state displacement d_s, i.e., $F_n(ds) > 0$, it can 'read' the current state and move the column through the bifurcation position $2\delta_0$ in x-direction, with $\delta_0 = L_c \sin\phi_0$. Thus, in configuration (3), the following should be satisfied,

$$F_n(d_s + 2\delta_0) = F_p \geq 2k_c\phi_0, \tag{1}$$

which is denoted as criteria C_1. Lastly, in configuration (4), an input displacement creates a buckling deformation along the positive x-direction, thereby generating compression in the spring. Then, when the input is maximal, $u_{in} = U_{max}$, the compression force should exceed the critical load of $F_{cr,2}$, and the state element switches back to the initial state-0.

Through the four points (1)-(4) in Fig. 1C, a continuous function, which represents the force–displacement characteristics of the connecting spring, can be plotted. The simplest function passing through these points is a cubic function, as indicated by the dashed line. We note that higher-order polynomial functions also fit through the four points, which leads to higher-order polynomials that describe the spring stiffness. We opted for the cubic form for ease of analysis and to gain clearer insights into the requirements of the nonlinear spring. Therefore, the stiffness of the connecting spring can be effectively characterized by a quadratic form, and be described by

$$k_n(u_n) = \alpha(u_n - r_1)(u_n - r_2), \tag{2}$$

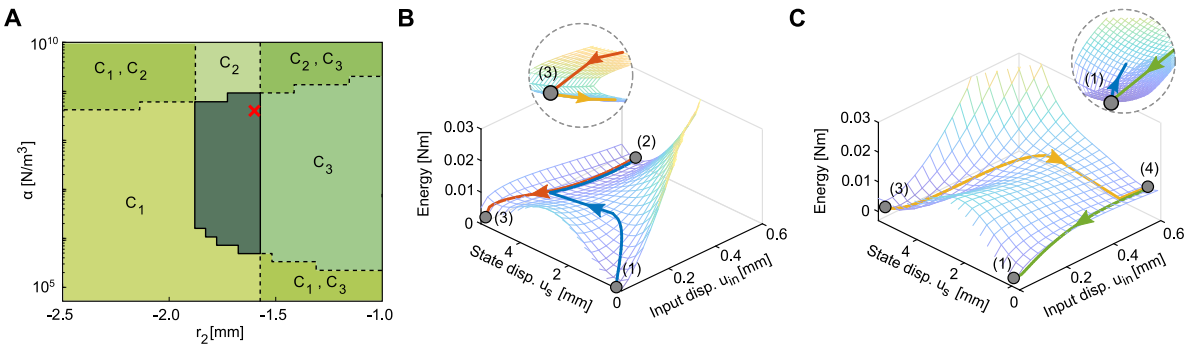

Fig. 2. Analytical case study. (A) Analysis of design parameters α and r_2 for the nonlinear spring. The center dark green region represents feasible combinations, while the surrounding regions fail to meet one or more of design criteria C_1, C_2, and C_3. The red cross indicates the values chosen for the case study. The energy landscape of the two bifurcation paths combined with the path of minimal energy from (B) state-0 and from (C) state-1. An offset of 0.1 mm in u_s-direction is given for the visibility of both paths. The zoom-ins at (1) and (3) show the switching between bifurcation energy landscapes. (For interpretation of the references to color in this figure legend, the reader is referred to the web version of this article.)

with u_n the spring displacement, and unknown variables α, r_1, and r_2. To get the nonlinear force response (F_n), Eq. (2) can be integrated. In the initial configuration ($u_n = 0$) the force $F_n(0) = 0$, thus integrating Eq. (2) yields

$$F_n(u_n) = \frac{\alpha u_n}{6}(2u_n^2 - 3r_1u_n - 3r_2u_n + 6r_1r_2). \tag{3}$$

However, not every value for α, r_1, and r_2 provides a viable solution. Namely, When the input is removed between config. (2) and (3), $u_{in} : U_{max} \rightarrow 0$, state-1 should remain in its stable position. This can be achieved under the condition that

$$F_n(u_n) > F_{cr,2} \quad \forall\, u_n \in [(2),(3)], \tag{4}$$

which is denoted as criteria C_2. Furthermore, there are no stresses in the initial configuration, and thus configuration (1) should be the lowest energy state. The energy of the connecting spring can be determined by integrating Eq. (3). In the initial configuration ($u_n = 0$) the potential energy $E_n(0) = 0$, thus integrating Eq. (3) yields

$$E_n = \frac{\alpha u_n^2}{12}(u_n^2 - 2r_1u_n - 2r_2u_n + 6r_1r_2) \geq 0 \quad \forall\, u_n, \tag{5}$$

which is denoted as criteria C_3.

To find viable nonlinear spring characteristics, an analysis is performed to find adequate combinations of design parameters α, r_1, and r_2 that satisfy Eqs. (1), (4), and (5), denoted as criteria C_1, C_2, and C_3, respectively. This analysis together with an analytical case study is presented in Section 3.

3. Analytical case study

We conducted an analytical case study to explore the characteristics of the nonlinear spring, with a particular focus on the design parameters α, and r_2, and their impact on the overall behavior of the mechanism. The value for r_1 is attributed to the properties of the state element, which is discussed later in this section. We first identify which force–deflection profile satisfies the predetermined criteria C_1, C_2, and C_3, as defined in Eqs. (1), (4), and (5), respectively. Additionally, we explored how a feasible force–deflection profile of the nonlinear spring that meets these criteria affects the performance of the proposed building block, such as the input displacement required for state switching and the corresponding input force.

For the analysis, we have chosen a state element with $L_s = 21$ mm, $\theta_0 = 7°$, $k_s = 1.735 \times 10^5$ N m^{-1}, a buckling column with $L_c = 2.1L_s$ for sufficient geometrical advantage, and an imperfection of $\phi_0 = 0.57°$ to enforce buckling in negative x-direction. Furthermore, rotational stiffness value k_c, with the hinges that can potentially be replaced by short-length flexures, and be described by

$$k_c = 4\frac{Ewt^3}{12L}, \tag{6}$$

with Young's modulus $E = 1.7$ GPa, width $w = 7.5$ mm, thickness $t = 0.5$ mm, and length $L = 4$ mm of the short-length flexures in the buckling column. To satisfy Eq. (1), it is reasonable to position the local maxima of Eq. (3) at point (3) in Fig. 1C, i.e., $r_1 = -(d_s + 2\delta_0)$, such that the greatest force can be delivered. However, it is not essential for point (3) to be at the local maximum; the primary requirement is the fulfillment of criteria C_1. In physical representations of the mechanism, precisely positioning the local maximum F_p of the connecting spring at $d_s + 2\delta_0$ might be challenging. Therefore, it may be more practical to use an accurate value of u_n to describe the displacement to local maximum d_p. This can be expressed as $d_p = d_S + 2\delta_0 \pm \epsilon$, where ϵ represents a small margin of error, assumed to be zero in the analytical model.

The analysis results for α and r_2 are presented in Fig. 2A. Several distinct regions can be identified, labeled with the corresponding criteria that are not satisfied. Firstly, three vertical regions that are dependent on the energy landscape of the nonlinear spring. When $r_2 < -1.87\,\text{mm}$, the energy landscape of the nonlinear spring shows only 1 stable point, indicating it cannot provide enough pull-in force, thus criteria C_1 is not satisfied. When $r_2 > -1.57\,\text{mm}$, the energy landscape becomes non-feasible because the energy at the second stable point drops below zero, thus criteria C_3 is not satisfied. Furthermore, within the range of $-1.87\,\text{mm} < r_2 < -1.57\,\text{mm}$, three distinct horizontal regions can be identified. Firstly, when $\alpha \gtrsim 6 \times 10^8\,\text{N m}^{-3}$, criteria C_2, i.e., Eq. (4), is not satisfied, resulting in the second state remaining unstable. Secondly, when $\alpha \lesssim 7 \times 10^5\,\text{N m}^{-3}$, criteria C_1, i.e., Eq. (1), is not satisfied, this implies that the connecting spring does not generate enough tension to pull the buckling column to the alternate bifurcation path. A combination of design parameters in the center region fulfills all constraints and can be selected for an analytical case study.

The performance of our building block can be evaluated using the criteria on the design parameters of the connecting spring. The spring stiffness is defined as $k_n = \alpha(u_n - r_1)(u_n - r_2)\text{N m}^{-1}$, where $\alpha = 4 \times 10^8\,\text{N m}^{-3}$, $r_1 = -(ds + 2\delta_0)$ m, and $r_2 = -1.6 \times 10^{-3}$ m. These values, indicated with a red cross in Fig. 2A, represent the physical prototype discussed in Section 4.

The total energy of the system (E_t) can be calculated by summing the energy of the connecting spring (E_n, as described in Eq. (5)), the state element (E_s), and the buckling column (E_c). These energy components can be derived from the spring-based rigid-body model. The energy landscapes of the left and right buckling bifurcation paths are illustrated in Figs. 2B and 2C, respectively. Additionally, the path of minimal energy for a full input cycle of $u_{in} = 0 \rightarrow U \rightarrow 0 \rightarrow U$, where U represents the maximal input displacement, is overlaid. The blue line represents the transition from 1 to 2, the red line from 2 to 3, the yellow line from 3 to 4, and the green line from 4 back to 1. This path is calculated using:

$$\nabla \mathcal{L} = 0, \quad \mathcal{L}(u_{in}, u_s, \lambda) = E_t + \lambda g, \tag{7}$$

where E_t represents the total potential energy, g denotes a constraint for the input displacement u_{in}, and λ is the input force required to maintain this constraint. The analysis suggests that our mechanism is capable of switching between the two states using a single digital input. When an input displacement is given, there is a sudden snap-through to a lower energy path, see (1) to (2) in Fig. 2B and (3) to (4) in Fig. 2C. This path remains stable even when the input is removed, see (2) to (3) and (4) to (1) in Figs. 2B and 2C, respectively. Upon reaching the new stable position, the opposite bifurcation path becomes the lowest energy path, leading the system to follow the alternate path upon the application of a new input displacement. This switching behavior, in (3) and (1), is evident in the zoom-ins, see Fig. 2D. After completing the full cycle, state-0 is reattained.

Using the spring-based rigid-body model, the influence of design parameters α and r_2 on the mechanism's performance can be readily evaluated, and depicted in Fig. 3. We analyzed four decreasing values for α (4, 3, 2, and 1×10^8) and r_2 (-1.60, -1.65, -1.70, and -1.75×10^{-3}). The analysis indicates that a lower value of α results in a decreased input force while a larger input displacement is necessary for state switching. This can be explained by the fact that α is a scalar of the stiffness function, see Eq. (2). Therefore, a larger input displacement is required to overcome the critical load of the state element but with a greater transmission ratio, i.e., decreased input force. Additionally, according to Fig. 3C and 3D, the influence of r_2 appears to be minimal and determines if the mechanism functions as desired.

4. Compliant design, numerical modeling, and fabrication

To experimentally validate our design method, we designed an elastic, planar embodiment where all rotational hinges are replaced with small-length flexures. The proposed compliant embodiment is shown in Fig. 4A, and labeled with the design parameters. The small-length flexures have a length of $L_f = 4\,\text{mm}$, and the thickness, t_f, was minimized to $0.5\,\text{mm}$, the minimum allowed by our fabrication method, to decrease strain energy during deformation and ensure the bistability of the design is not negatively impacted [56]. The mechanism's out-of-plane thickness, denoted as p_s, was set at $7.5\,\text{mm}$. Additionally, the thickness of the rigid beams in the bistable elements, represented by t_b, was fixed at $2\,\text{mm}$, while t_c was maintained at $5.5\,\text{mm}$ to provide sufficient stiffness. For the state element, we used two parallel bistable trusses to provide rectilinear translation. For the connecting spring, we chose a single bistable truss due to its cubic force–displacement behavior. The buckling column is converted to a compliant embodiment by replacing the rotational hinges with three small-length flexures, and with an imperfection δ_0 to enforce buckling. In addition, the column is suspended on a compliant shuttle to allow for rectilinear input displacement. A prototype is fabricated using 3D printing by Multi Jet Fusion (MJF) using polyamide-12 (Nylon-12), shown in Fig. 4B, with annotated regions that represent the state element, connecting spring, buckling column, and a region indicating one of the compression springs k_s.

Finite element analysis (FEA) using Ansys Parametric Design Language (APDL) was conducted to dimension the compliant embodiment and verify its performance when combining the three elements. Two-node beam elements (beam188), based on Timoshenko beam theory, with rectangular beam cross-section, were used. The mechanism's material parameters are: Young's modulus $E = 1.7\,\text{GPa}$, density $\rho = 1010\,\text{kg m}^{-3}$, and Poisson's ratio $\nu = 0.33$ [57]. The mechanism is anchored with fixed boundary conditions at the points where it interfaces with the frame, see Fig. 6A. The design parameters were carefully selected to ensure the maximum Von Mises stress remained below the $48\,\text{MPa}$ limit, thereby maintaining the mechanism's structural integrity.

The appropriate dimensions for the state element were determined through a parametric study, in accordance with the design guidelines outlined in the previous section. Within this study, parameters such as w_s, L_s, and θ_s (as illustrated in Fig. 5A (1)), were varied for careful selection. The parameter h_s was maintained constant at a value of $1.5\,\text{mm}$ due to the resolution of the fabrication technique. This is particularly relevant as h_s is cubically proportional to the support stiffness k_s, while w_s exhibits an inverse cubic proportionality, as detailed in see Eq. (8).

$$k_s = \frac{3 E p_s h_s^3}{12 w_s^3}, \tag{8}$$

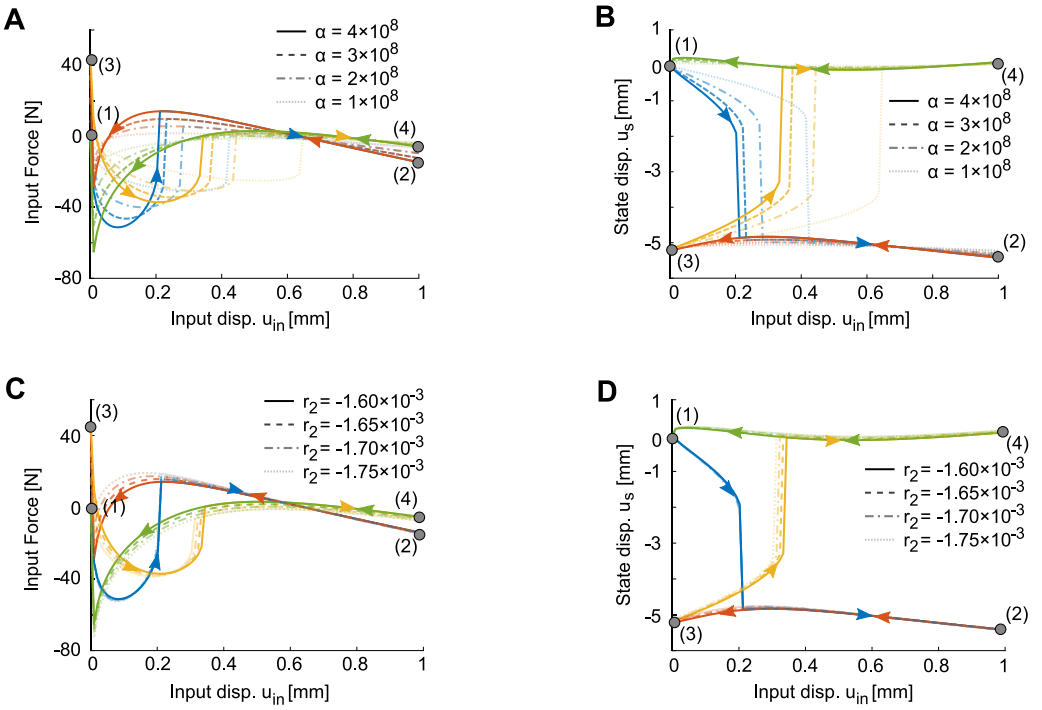

Fig. 3. Performance analysis with different values of α and r_2. The blue lines show behavior from config. 1 to 2, the red lines from config. 2 to 3, the yellow lines from config. 3 to 4, and the green lines from config. 4 back to 1. The force–displacement characteristics for different values of (A) α and (C) r_2, respectively. The input–output displacement for different values of (B) α and (D) r_2, respectively. (For interpretation of the references to color in this figure legend, the reader is referred to the web version of this article.)

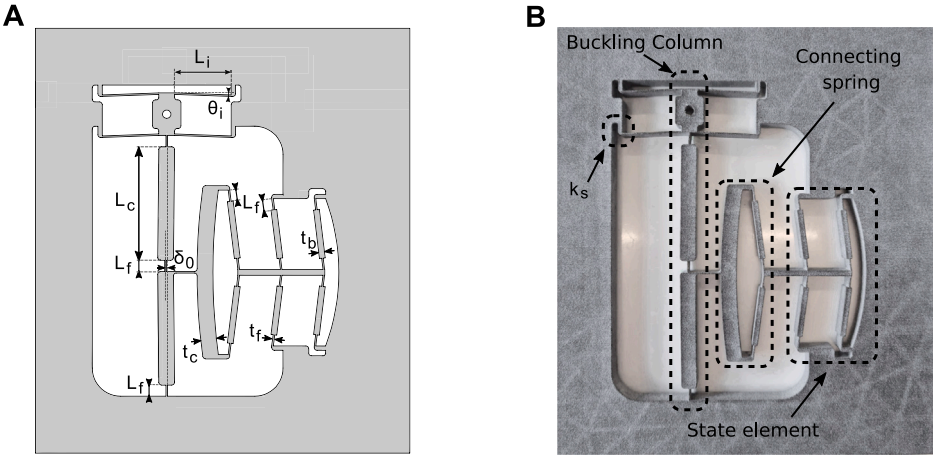

Fig. 4. (A) Proposed compliant embodiment of the building block, labeled with design parameters. (B) Fabricated prototype, labeled with the main elements. The proposed design has a out-of-plane thickness of 7.5 mm, all flexures have a length of 4 mm and thickness of 0.5 mm, all compression springs (k_s) have a length of 3.5 mm and thickness of 1.5 mm, and all beams have a thickness of 5.5 mm.

with E representing the materials Young's modulus. The analysis included examination of critical loads $F_{cr,1}$ and $F_{cr,2}$, along with the displacement between the two equilibrium positions d_s, see Fig. 5A (2), (3), and (4), respectively. A lower limit was imposed with a blue line where the element is not bistable, and an upper limit was imposed on critical load $F_{cr,1}$ with a red line to adhere to a stress limit in the buckling column. A preliminary simulation of the buckling column indicated a maximum force $F_{cr,1}$ of 6 N, serving as a guideline to prevent exceeding the stress limit; subsequent design of the column when selecting the state element should ensure compliance with this constraint. The primary plots display the data for $\theta_s = 7°$, while for $\theta_s = 6°$ and $\theta_s = 8°$ only the lower and upper limit are displayed with dotted and dashed lines, respectively. The chosen design - indicated with blue star with parameters $w_s = 3.5$ mm $L_s = 17.13$ mm, and $\theta_s = 7°$ - satisfy the lower and upper limit.

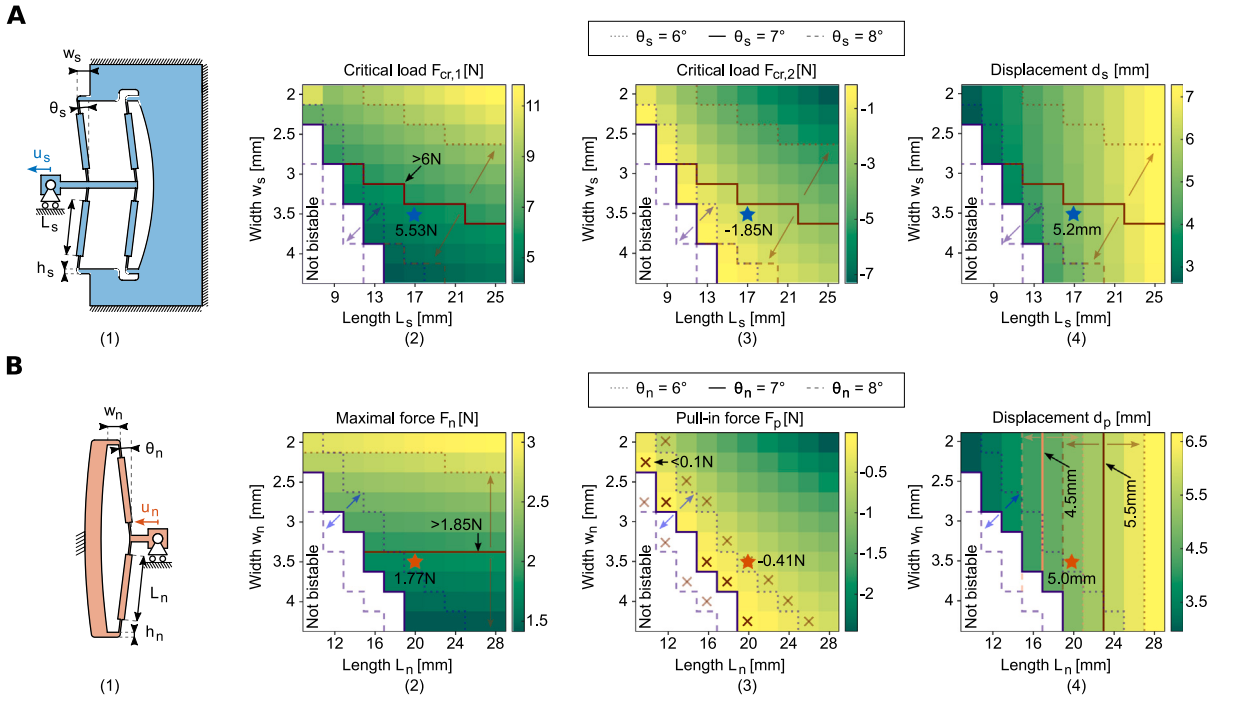

Fig. 5. Parametric study of the state element and connecting spring. (A) The geometrical design of the state element is presented in (1). The results of the FEA for Critical loads $F_{cr,1}$ and $F_{cr,2}$ are shown in (2) and (3), respectively, and with the displacement between the two equilibrium positions d_s depicted in (4). (B) The geometrical design of the connecting spring is illustrated in (1). The FEA results covering the maximal force F_n, pull-in force F_p, and the input displacement d_p are presented in (2), (3), and (4), respectively. (For interpretation of the references to color in this figure legend, the reader is referred to the web version of this article.)

After selecting the dimensions for the state element, a subsequent parametric study, see Fig. 5B, was undertaken to determine the dimensions of the connecting spring. The parameter h_n was fixed to the same value as h_s, while parameters w_n, L_n, and θ_n were systematically varied. This approach aimed to find combinations that ensure compliance with the criteria outlined in Section 2. Criterion 3, see Eq. (5), which ensures that the energy in the connecting spring is equal to or greater than zero, is automatically satisfied when moving from theoretical model to physical embodiment. Criterion 2, see Eq. (4), states that the first critical load of the connecting spring, F_n, should be lower (in absolute value) than the second critical load of the state element $F_{cr,2}$. Therefore, there is an upper limit for the maximal force set at $F_n \leq 1.85\,\text{N}$, as shown by the red line in Fig. 5B (2). The maximal force F_n is highly influenced by the angle θ_n, as shown by the shifted upper limit with dotted and dashed lines for $\theta_n = 6°$ and $\theta_n = 8°$, respectively. According to Criterion 1, see Eq. (1), the tensile force F_p produced by the connecting spring should be equal to or greater than the force generated by the hinges of the buckling column when displacing the buckling column to the other buckling direction, i.e., $2\delta_0$. A preliminary simulation of the buckling column was performed in which the point where the connecting spring attaches to the column was displaced $2\delta_0 = 0.8\,\text{mm}$. The results indicated that the hinges in the buckling column produce a force of $0.1\,\text{N}$, which served as a guideline for the design. This eliminates certain parameter combinations indicated with a cross, see Fig. 5B (3). Faded crosses are used to indicate the eliminated combinations for $\theta_n = 6°$ and $\theta_n = 8°$. Furthermore, to satisfy criterion 1, the force F_p should be applied at an input displacement of $u_n = d_p = d_s + 2\delta_0 \pm \epsilon$, with $\epsilon \approx 0$. In our analysis, $\epsilon \leq 0.1 d_s$, which is indicated in Fig. 5B(4) with solid pink and brown lines for $\theta_n = 7°$ and dotted and dashed lines for $\theta_n = 6°$ and $\theta_n = 8°$, respectively. This results in a lower and upper limit for L_n. The chosen design - indicated with an orange star with parameters $w_n = 3.5\,\text{mm}$, $L_n = 20.15\,\text{mm}$, and $\theta_n = 7°$- fulfills the three criteria and has similar values for α, r_1, and r_2 as mentioned in Section 3.

To find satisfactory dimensions of the buckling column, we first determined a target input displacement. Our target was an input displacement of $0.8\,\text{mm}$ and in combination with the selected state displacement d_s of $5.2\,\text{mm}$, the buckling column requires a transmission ratio of 6.5. Based on Fig. 1A, we estimated the length L_c for our design. The buckling column, with a length $L_c = 40\,\text{mm}$, with a transmission ratio of 7, effectively displaces the state element by a distance d_s. Subsequently, we evaluated the thickness and length of the short-length flexures to ensure that the stress within the mechanism remains within acceptable limits. The final design has a length $L_c = 40\,\text{mm}$, and an imperfection $\delta_0 = 0.4\,\text{mm}$. Finally, to accommodate input displacement in the y-direction, the input shuttle is suspended with four angled flexures, with length $L_i = 20\,\text{mm}$, and $\theta_i = 2°$ to handle the input displacement within the stress limit.

Experiments were carried out to assess the force–displacement characteristics and input–output kinematics of the mechanism. For the force–displacement measurement, a 45N force sensor (Futek LSB200 FSH03878), mounted to a precision linear stage (PI M505) is used. An input displacement of $1.2\,\text{mm}$ was applied to the input shuttle of the mechanism. Simultaneously, for the input–output

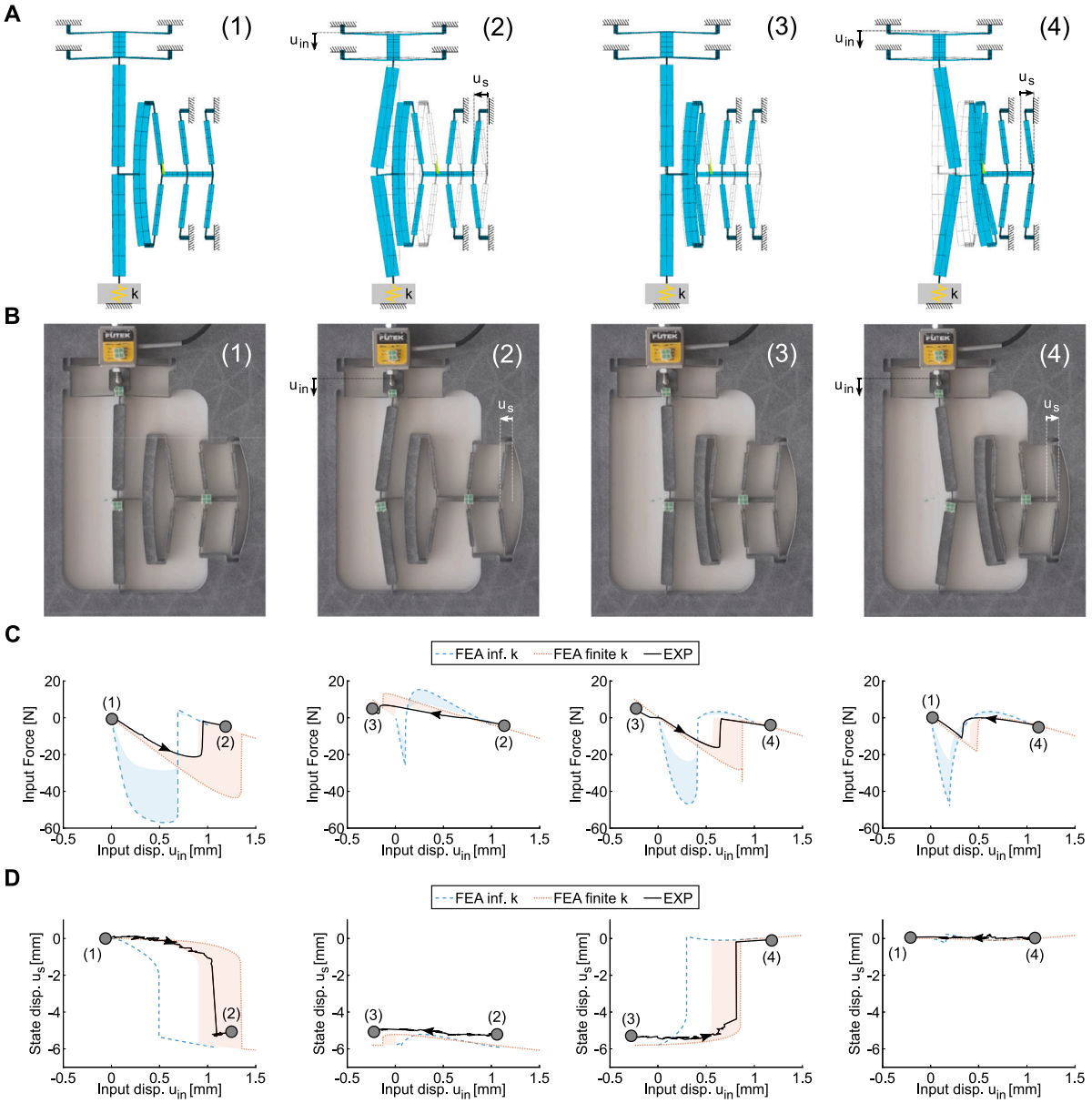

Fig. 6. FEA and experimental results. Snapshots illustrating the four configurations of the mechanism upon applying a cyclic digital input displacement for (A) the FEA model and (B) the fabricated prototype. (C) Force–displacement characteristics for each transition with shaded region representing decreasing Young's modulus until 0.85 GPa. (D) Input–output kinematics for each transition with shaded region representing decreasing Young's modulus until 0.85 GPa.

displacement measurement, the displacement of the input shuttle and state element is captured using a video camera and then analyzed using image processing.

5. Results and discussion

Measurement (EXP) and finite element simulation (FEA) results of our compliant embodiment are shown in Fig. 6. Four distinct configurations of the FEA model and the fabricated mechanism throughout different sequences are shown in Fig. 6A and 6B, respectively. For a video of the mechanism in action, see video S1 in the supplementary material. The configurations at each stage are denoted as (1), (2), (3), and (4), respectively. As can be seen, simulations are in good agreement with the captured deformations. The transition from configuration (1) to (2) illustrates the buckling of the column along with the state switching to state-1. In the transition from configuration (2) to (3), the state's stability is evident, while the nonlinear spring delivers a tensile force on the buckling column. Due to the tension in the connecting spring, the buckling column follows the second bifurcation path, i.e., along the

positive x-direction, upon applying an input displacement. This action prompts the transition from configuration (3) to (4), causing the state to reset to its original state-0 position. A tilt of the nonlinear spring is observed in a similar direction in both simulation and experiment. The flexure connecting the nonlinear spring and column is moved slightly downwards due to the buckling of the column. The resultant force is therefore slightly off-center, causing the rotation of the nonlinear spring. Lastly, in the transition from configuration (4) to (1), upon removing the input displacement, the state remains stable, and the mechanism arrives in its original configuration. In our finite element model, we also incorporate a virtual spring at the clamping point of the buckling column with stiffness K as illustrated in Fig. 6A. This approach allows us to later investigate the sensitivity of our mechanism to the flexibility caused by our experimental setup and the grounding frame.

Fig. 6C and 6D present the force–deflection characteristics and input–output relation obtained from EXP and FEA. The dimensions of the FEA-model were updated based on the measurements taken from the fabricated prototype. The dimensions were measured with an accuracy of 0.25 mm and were as follows: $L_s = 17.5\,\text{mm}$, $w_s = w_n = 3.75\,\text{mm}$, $h_s = h_n = 1.5\,\text{mm}$, $\theta_s = 7.75°$, $L_n = 20.5\,\text{mm}$, and $\theta_n = 8°$. The results from the updated FEA model are depicted with blue dashed lines. The input sequence corresponds to an input displacement pattern of $u_{in} = 0\,\text{mm} \rightarrow 1\,\text{mm} \rightarrow 0\,\text{mm} \rightarrow 1\,\text{mm}$. In this simulation, we consider infinitely stiff boundary conditions, i.e. virtual spring $k = \infty$, which excludes the flexibility of our measurement setup. Furthermore, the black lines represent experimental measurements, where an input displacement pattern of $u_{in} = -0.2\,\text{mm} \rightarrow 1.2\,\text{mm} \rightarrow -0.2\,\text{mm} \rightarrow 1.2\,\text{mm}$ were applied during measurement.

As can be observed, discrepancies exist between the EXP and the FEA results, both in terms of the input displacement required for switching and corresponding actuation forces. These discrepancies were attributed to the finite stiffness of the prototype's frame, the measurement setup, and uncertainties in Young's modulus. To address this, we performed force–deflection measurements on the frame in the setup, yielding a setup stiffness of $4.5 \times 10^4\,\text{N m}^{-1}$. We later incorporated this value in our FEA model by adjusting the virtual stiffness to the measured value. The results of this modification are shown with the dashed orange lines. As can be seen, now the state switching occurs with an input displacement pattern of $u_{in} = -0.2\,\text{mm} \rightarrow 1.52\,\text{mm} \rightarrow -0.2\,\text{mm} \rightarrow 1.52\,\text{mm}$. In addition, the prototypes were fabricated using Material Jet Fusion (MJF); while it should be possible to fabricate flexures of 0.5 mm using this method, a closer examination of the prototypes revealed heterogeneous material filling within the flexures. This does not accurately reflect the material properties used in the simulations. Therefore, for both FEA models, simulations were conducted using a lower Young's modulus of 0.85 GPa. The results are indicated with shaded areas. The results of the force–deflection simulations and measurements show similar behavior as the analytical model, see Fig. 3.

Fig. 6C displays the force–deflection results, where the arrows indicate the direction. The required input force switching to state-1, transition from configuration (1) to (2), is between −28.5 N and −57.0 N in simulation with infinite k, and between −21.5 N and −43.5 N in simulation with $k = 4.5 \times 10^4$, this is compared to −21.3 N in our experimental measurements. Next, when removing the input, transition from configuration (2) to (3), a maximal force of between 7.7 N and 15.4 N in simulation with infinite k, and between 6.5 N and 13.2 N in simulation with $k = 4.5 \times 10^4$ is reached, compared to 6.9 N in the experiment. Then, for switching back to state-0, transition from configuration (3) to (4), a force between −23.4 N and −46.8 N in simulation with infinite k, and between −14.0 N and −28.3 N in simulation with $k = 4.5 \times 10^4$, compared to −16.2 N in the experiment is needed. Lastly, returning to the original configuration, transition from configuration (4) to (1), the peak force is between −22.6 N and −47.5 N in simulation with infinite k, and between −13.5 N and −18.4 N in simulation with $k = 4.5 \times 10^4$, compared to −11.1 N in the experiment.

The input–output displacement results derived from both simulation and experiment are displayed in Fig. 6D. Similarly, the arrows indicate the direction of the lines. The y-axis displays the state displacement, where 0 mm displacement represents state-0 and ∼ 5 mm represents state-1. A sudden snap-through can be observed in transition (1) to (2) from state-0 to state-1 and vice-versa in transition (3) to (4), after the snap-through the state displacement remains stable when the input displacement is removed; this behavior is the state-switching. For the transition from configuration (1) to (2), an input displacement u_{in} results in a state displacement u_s of 5.4 mm in simulation with infinite k, and 6.0 mm in simulation with $k = 4.5 \times 10^4$ compared to 5.3 mm in experiments to state-1. The snap-through is triggered at an input displacement of 0.49 mm in simulation with infinite k (note that the Young's modulus has no influence), and between 0.91 mm and 1.29 mm in simulation with $k = 4.5 \times 10^4$ compared to 1.0 mm in experiments. The state then retains this position when the input is removed, the transition from configuration (2) to (3), until a subsequent input is applied. The next input displacement u_in causes the transition from configuration (3) to (4), upon which the state resets back to state-0 at 0 mm for both simulation and experiment. The snap-through occurs at an input displacement of 0.30 mm in simulations with infinite k, and between 0.57 mm and 0.87 mm in simulation with $k = 4.5 \times 10^4$ compared to 0.83 mm in the experiment.

Further observed discrepancies between the measurements and simulations can potentially be attributed to the finite stiffness of the frame, which is not considered in the FEA besides the implemented virtual spring with stiffness k(4.5×10^4). Bistable structures are highly sensitive to boundary conditions. When boundary conditions are overly compliant, bistability may be lost entirely. Precautions have been taken to increase the frame's stiffness. Such as taping the prototype to a PMMA base plate, however, small changes in the boundary conditions, such as small outward displacement of the boundary conditions of the state element due to flexion of the frame, can explain some of the discrepancies. From the sensitivity analysis, it was determined that the behavior of the mechanism is dominated by the state element. An estimation of our frame in-plane stiffness at the state element is $3 \times 10^5\,\text{N m}^{-1}$, which is in series connection to support stiffness k_s, see Figs. 1A and 4A. The support stiffness k_s is estimated to be $1.735 \times 10^5\,\text{N m}^{-1}$, thus the frame stiffness contributes significantly, further explaining the differences observed.

Lastly, to actuate the mechanism, a hole of 3 mm in diameter was implemented in the prototype to accommodate a hook attachment to provide input displacement. Due to the difference in diameter of the hole and hook, there was some hysteresis of ∼ 0.1 mm in the measurement, this can be seen around 0.7 mm and 0 mm at 0 N in Fig. 6C(2) and (3), respectively.

6. Opportunities and outlook

In this study, our primary focus was on the quasi-static behavior of the mechanism, with the dynamic characteristics remaining unexplored. For instance, material selection is crucial due to inherent visco-elastic behavior. As the mechanism approaches the snap-through point, the visco-elasticity can lead to relaxation behavior, thereby changing the precise snapping moment. This phenomenon becomes particularly significant during the transition from configuration 2 to configuration 3, where the forces involved are relatively low. Due to this phenomenon, besides hysteresis, we applied a small negative displacement of $u_{in} = -0.2\,\mathrm{mm}$ to our mechanism in the experimental study. Furthermore, to comprehensively understand the dynamic performance of the mechanism, it might be beneficial to further explore its maximum operating frequency through a multi-body dynamic model.

When adapting our single digital input state-switching mechanism for real-world applications where an output load is required, careful consideration of load placement becomes crucial. To maintain the mechanism's desired bistable behavior and eliminate unintended state changes, the output load should preferably be placed on the buckling column, e.g., at the left/right buckling point, rather than directly on the state element.

Furthermore, an interesting observation is that the input–output displacement relation of our mechanism exhibits characteristics of a frequency divider, see Fig. 6D and E. In MEMS devices, operation frequencies from actuators are generally high. While mechanical frequency up-conversions have been achieved before [58,59], down-conversion of motion frequency is rarely reported. By concatenating multiple instances of our building block – and considering that the loads transmitted through such a system should still be carried by the input beam – we could potentially achieve higher frequency division ratios.

Lastly, while this study outlines design guidelines for the proposed mechanism, it is important to highlight the generality of our approach. To illustrate the feasibility of our design principle, we fabricated a prototype that satisfies the design criteria. However, these guidelines are not confined to this specific embodiment. For instance, our prototype embodies a rectilinear input displacement and bistable mechanism, but our design principle can adapt to other design embodiments, including rotational input displacement and other variants of bistable elements. Moreover, while our prototype is realized at the decimeter scale, the framework we present holds potential across a range of length scales, from nano to macro. Thus, our demonstrated prototype serves as a tangible representation, but our design guidelines are applicable more broadly, offering adaptation beyond the embodiment we present.

7. Conclusion

We have presented a fully elastic state-switching mechanism that can convert a cyclic digital input signal into two distinct stable states. This functionality is achieved by harnessing internal instability that guides the bifurcation path of a buckling column. By 'reading' the mechanism's current state, and 'writing' the input into the state element, it facilitates alternating switching behavior. In contrast to previous studies in which state switching has been achieved through complex contact-based interaction, we laid out a guideline for designing nonlinear springs that facilitate state switching through a fully elastic and monolithic embodiment. Although we demonstrated the theory using a centimeter-scale prototype in this study, it is important to note that our approach is compatible with miniaturization, suitable for a broad spectrum of applications, from micro switches to reprogrammable metamaterials. Furthermore, the proposed methodology allows for different variations, such as changing the nature of the input motion, e.g., the type of displacement field, or adjusting the readout mode. Lastly, while this work focused on a system characterized by a single digital input and state element, the strategy lays the groundwork for the development of flexible mechanisms with sequencing behavior, such as sequencing between parallel sets of state elements through a single digital input.

CRediT authorship contribution statement

Malte A. ten Wolde: Writing – review & editing, Writing – original draft, Visualization, Validation, Project administration, Methodology, Investigation, Formal analysis, Data curation. **Davood Farhadi:** Writing – review & editing, Writing – original draft, Visualization, Supervision, Resources, Project administration, Methodology, Investigation, Funding acquisition, Conceptualization.

Declaration of competing interest

The authors declare that they have no known competing financial interests or personal relationships that could have appeared to influence the work reported in this paper.

Data availability

No data was used for the research described in the article.

Acknowledgment

We acknowledge funding support from Dutch research council (NWO-ENW Rubicon Grant 019.191EN.022, 2019).

Appendix A. Supplementary data

Supplementary material related to this article can be found online at https://doi.org/10.1016/j.mechmachtheory.2024.105626.

References

[1] Y. Cao, M. Derakhshani, Y. Fang, G. Huang, C. Cao, Bistable structures for advanced functional systems, Adv. Funct. Mater. 31 (45) (2021) 2106231.
[2] R. Xu, C. Chen, J. Sun, Y. He, X. Li, M.-H. Lu, Y. Chen, The design, manufacture and application of multistable mechanical metamaterials-a state-of-the-art review, Int. J. Extrem. Manuf. (2023).
[3] T. Chen, O.R. Bilal, K. Shea, C. Daraio, Harnessing bistability for directional propulsion of soft, untethered robots, Proc. Natl. Acad. Sci. 115 (22) (2018) 5698–5702.
[4] Y. Tang, Y. Chi, J. Sun, T.-H. Huang, O.H. Maghsoudi, A. Spence, J. Zhao, H. Su, J. Yin, Leveraging elastic instabilities for amplified performance: Spine-inspired high-speed and high-force soft robots, Sci. Adv. 6 (19) (2020) eaaz6912.
[5] T. Chen, M. Pauly, P.M. Reis, A reprogrammable mechanical metamaterial with stable memory, Nature 589 (7842) (2021) 386–390.
[6] Y. Zhang, Q. Wang, M. Tichem, F. van Keulen, Design and characterization of multi-stable mechanical metastructures with level and tilted stable configurations, Extreme Mech. Lett. 34 (2020) 100593.
[7] A. Rafsanjani, D. Pasini, Bistable auxetic mechanical metamaterials inspired by ancient geometric motifs, Extreme Mech. Lett. 9 (2016) 291–296.
[8] T. Chen, J. Panetta, M. Schnaubelt, M. Pauly, Bistable auxetic surface structures, ACM Trans. Graph. 40 (2021) 1–9.
[9] H. Yang, L. Ma, 1D to 3D multi-stable architected materials with zero Poisson's ratio and controllable thermal expansion, Mater. Des. 188 (2020) 108430.
[10] L. Jin, R. Khajehtourian, J.H. Mueller, A. Rafsanjani, V. Tournat, K. Bertoldi, D.M. Kochmann, Guided transition waves in multistable mechanical metamaterials, Proc. Natl. Acad. Sci. 117 (2020) 2319–2325.
[11] U. Waheed, C. Myant, S. Dobson, Boolean AND/OR mechanical logic using multi-plane mechanical metamaterials, Extreme Mech. Lett. 40 (2020) 100865.
[12] P.R. Kuppens, M.A. Bessa, J.L. Herder, J.B. Hopkins, Monolithic binary stiffness building blocks for mechanical digital machines, Extreme Mech. Lett. 42 (2021) 101120.
[13] M. Zanaty, H. Schneegans, I. Vardi, S. Henein, Reconfigurable logic gates based on programable multistable mechanisms, J. Mech. Robotics 12 (2) (2020) 021111.
[14] D.J. Preston, P. Rothemund, H.J. Jiang, M.P. Nemitz, J. Rawson, Z. Suo, G.M. Whitesides, Digital logic for soft devices, Proc. Natl. Acad. Sci. 116 (16) (2019) 7750–7759.
[15] S. Shan, S.H. Kang, J.R. Raney, P. Wang, L. Fang, F. Candido, J.A. Lewis, K. Bertoldi, Multistable architected materials for trapping elastic strain energy, Adv. Mater. 27 (29) (2015) 4296–4301.
[16] Q. Xu, Design of a large-stroke bistable mechanism for the application in constant-force micropositioning stage, J. Mech. Robotics 9 (1) (2016).
[17] Y. Gerson, S. Krylov, B. Ilic, D. Schreiber, Design considerations of a large-displacement multistable micro actuator with serially connected bistable elements, Finite Elem. Anal. Des. 49 (1) (2012) 58–69.
[18] M. Power, A. Barbot, F. Seichepine, G.-Z. Yang, Bistable, pneumatically actuated microgripper fabricated using two-photon polymerization and oxygen plasma etching, Adv. Intell. Syst. 5 (4) (2023) 2200121.
[19] W.-C. Chen, C. Lee, C.-Y. Wu, W. Fang, A new latched 2×2 optical switch using bi-directional movable electrothermal H-beam actuators, Sensors Actuators A 123–124 (2005) 563–569.
[20] J. Qiu, J. Lang, A. Slocum, A. Weber, A bulk-micromachined bistable relay with U-shaped thermal actuators, J. Microelectromech. Syst. 14 (5) (2005) 1099–1109.
[21] B. Yang, B. Wang, W.K. Schomburg, A thermopneumatically actuated bistable microvalve, J. Micromech. Microeng. 20 (9) (2010) 095024.
[22] S. Nummelin, B. Shen, P. Piskunen, Q. Liu, M.A. Kostiainen, V. Linko, Robotic DNA nanostructures, ACS Synth. Biol. 9 (8) (2020) 1923–1940.
[23] Y. Ke, C. Castro, J.H. Choi, Structural DNA nanotechnology: Artificial nanostructures for biomedical research, Annu. Rev. Biomed. Eng. 20 (1) (2018) 375–401.
[24] L. Zhou, A.E. Marras, H.-J. Su, C.E. Castro, Direct design of an energy landscape with bistable DNA origami mechanisms, Nano Lett. 15 (3) (2015) 1815–1821.
[25] I. Foulds, M. Parameswaran, Hysteresis spring single digital input bistable mechanism, in: 2005 International Conference on MEMS,NANO and Smart Systems, 2005, pp. 455–458.
[26] D. Melancon, A.E. Forte, L.M. Kamp, B. Gorissen, K. Bertoldi, Inflatable origami: Multimodal deformation via multistability, Adv. Funct. Mater. (2022) 2201891.
[27] P. Bhovad, J. Kaufmann, S. Li, Peristaltic locomotion without digital controllers: Exploiting multi-stability in origami to coordinate robotic motion, Extreme Mech. Lett. (2019) 100552.
[28] N. Hu, B. Li, R. Bai, K. Xie, G. Chen, A torsion-bending antagonistic bistable actuator enables untethered crawling and swimming of miniature robots, Res. Sci. Partn. J. (2023).
[29] J.R. Raney, N. Nadkarni, C. Daraio, D.M. Kochmann, J.A. Lewis, K. Bertoldi, Stable propagation of mechanical signals in soft media using stored elastic energy, Proc. Natl. Acad. Sci. (35) (2016) 9722–9727.
[30] Y. Zhang, M. Tichem, F. van Keulen, Concept and design of a metastructure-based multi-stable surface, Extreme Mech. Lett. 51 (2022) 101553.
[31] S. Janbaz, K. Narooei, T. van Manen, A.A. Zadpoor, Strain rate–dependent mechanical metamaterials, Sci. Adv. 6 (25) (2020) eaba0616, Publisher: American Association for the Advancement of Science.
[32] L.S. Novelino, Q. Ze, S. Wu, G.H. Paulino, R. Zhao, Untethered control of functional origami microrobots with distributed actuation, Proc. Natl. Acad. Sci. 117 (39) (2020) 24096–24101.
[33] A. Walther, Viewpoint: From responsive to adaptive and interactive materials and materials systems: A roadmap, Adv. Mater. 32 (20) (2020) 1905111.
[34] C. Kaspar, B.J. Ravoo, W.G. van der Wiel, S.V. Wegner, W.H.P. Pernice, The rise of intelligent matter, Nature 594 (7863) (2021) 345–355.
[35] D. Drotman, S. Jadhav, D. Sharp, C. Chan, M.T. Tolley, Electronics-free pneumatic circuits for controlling soft-legged robots, Science Robotics (2021).
[36] M. Sitti, Physical intelligence as a new paradigm, Extreme Mech. Lett. 46 (2021) 101340.
[37] M.A. McEvoy, N. Correll, Materials that couple sensing, actuation, computation, and communication, Science 347 (6228) (2015) 1261689, Publisher: American Association for the Advancement of Science.
[38] H. Yasuda, P.R. Buskohl, A. Gillman, T.D. Murphey, S. Stepney, R.A. Vaia, J.R. Raney, Mechanical computing, Nature 598 (7879) (2021) 39–48.
[39] R.N. Kent, Patent: Writing instrument, 1965.
[40] H.-W. Huang, Y.-J. Yang, A MEMS bistable device with push-on–push-off capability, J. Microelectromech. Syst. 22 (1) (2013) 7–9.
[41] B.L. Weight, L.L. Howell, S.M. Lyon, S.M. Wait, Two-Position Micro Latching Mechanism Requiring a Single Actuator, American Society of Mechanical Engineers Digital Collection, 2008, pp. 797–803.
[42] S.-W. Huang, F.-C. Lin, Y.-J. Yang, A novel single-actuator bistable microdevice with a moment-driven mechanism, Sensors Actuators A 310 (2020) 111934.
[43] Y. Gao, T. Ema, Z. Cao, S. Ni, E.Y.L. Chan, O. Tabata, T. Tsuchiya, X. Wang, M. Wong, A planar single-actuator bi-stable switch based on latch-lock mechanism, 2019, pp. 705–708.
[44] A. A. Zadpoor, Mechanical meta-materials, Mater. Horiz. 3 (5) (2016) 371–381, Publisher: Royal Society of Chemistry.
[45] M. Kadic, G.W. Milton, M. van Hecke, M. Wegener, 3D metamaterials, Nat. Rev. Phys. 1 (3) (2019) 198–210.
[46] L.J. Kwakernaak, M. van Hecke, Counting and sequential information processing in mechanical metamaterials, Phys. Rev. Lett. 130 (2023) 268204.
[47] H. Bense, M. van Hecke, Complex pathways and memory in compressed corrugated sheets, Proc. Natl. Acad. Sci. 118 (50) (2021) e2111436118.

[48] J.A. Faber, J.P. Udani, K.S. Riley, A.R. Studart, A.F. Arrieta, Dome-patterned metamaterial sheets, Adv. Sci. 7 (22) (2020) 2001955.
[49] K. Bertoldi, V. Vitelli, J. Christensen, M. van Hecke, Flexible mechanical metamaterials, Nat. Rev. Mater. 2 (11) (2017) 17066.
[50] C. Merrigan, D. Shohat, C. Sirote, Y. Lahini, C. Nisoli, Y. Shokef, Disorder, multistability, and mechanical memory in an ordered metamaterial, 2022, arXiv preprint arXiv:2204.04000.
[51] W.M. van Spengen, R. Puers, I. de Wolf, On the physics of stiction and its impact on the reliabilityof microstructure, J. Adhes. Sci. Technol. 17 (4) (2003) 563–582.
[52] D. Farhadi Machekposhti, N. Tolou, J. Herder, A review on compliant joints and rigid-body constant velocity universal joints toward the design of compliant homokinetic couplings, J. Mech. Des. 137 (3) (2015) 032301.
[53] C. Gosselin, J. Angeles, et al., Singularity analysis of closed-loop kinematic chains, IEEE Trans. Robot. Autom. 6 (3) (1990) 281–290.
[54] H.M. Daniali, P. Zsombor-Murray, J. Angeles, Singularity analysis of planar parallel manipulators, Mech. Mach. Theory 30 (5) (1995) 665–678.
[55] G.J. van den Doel, J.L. Herder, D. Farhadi, Harnessing elastic energy to overcome singularity issues in four-bar mechanisms with a crank link, Mech. Mach. Theory 183 (2023) 105274.
[56] S.A. Zirbel, K.A. Tolman, B.P. Trease, L.L. Howell, Bistable mechanisms for space applications, PLoS One 11 (2016) e0168218.
[57] A. Alomarah, S.H. Masood, I. Sbarski, B. Faisal, Z. Gao, D. Ruan, Compressive properties of 3D printed auxetic structures: experimental and numerical studies, Virtual Phys. Prototyping (2019) 1–21.
[58] D. Farhadi Machekposhti, J.L. Herder, G. Sémon, N. Tolou, A compliant micro frequency quadrupler transmission utilizing singularity, J. Microelectromech. Syst. 27 (3) (2018) 506–512.
[59] D. Farhadi Machekposhti, J.L. Herder, N. Tolou, Frequency doubling in elastic mechanisms using buckling of microflexures, Appl. Phys. Lett. 115 (14) (2019).